Supplementary Material: Exponentially enhanced sensing through nonreciprocal light propagation

P.-É. Blanchard,[1] A. McDonald,[2] and P. St-Jean[1,3]

[1] *Département de Physique, Université de Montréal, Montréal, Québec, Canada*
[2] *Institut Quantique and Département de Physique, Université de Sherbrooke, Sherbrooke, Québec, Canada*
[3] *Institut Courtois, Université de Montréal, Montréal, Québec, Canada*

I. EXPERIMENTAL METHOD

A. Experimental setup

A schematic of the the photonic platform used in this work is drawn in Fig. S1. We use a NKT Koheras ADJUSTIK laser source with a central tunable wavelength at 1550.12 nm and a linewidth < 100 Hz. An optical attenuator is used to limit the input drive amplitude and keep the setup in the linear regime. The output of the laser is split in three parts : a first part is guided to a heterodyne detection setup, a second is guided to the intensity modulator monitoring section, and the remaining power is injected in the main loop. A smaller secondary loop, around 0.3 m long, is coupled to the main one via a 25:75 coupler. Two modulators are placed within the main optical fiber loop : a phase modulator (PM) and an intensity modulator (IM), each driven from a Zurich Instruments High Definition Arbitrary Waveform Generator (HDAWG). All optical components in the setup are polarization maintaining to ensure perfect alignment with the optical axes of the electro-optical modulators; a polarizer is used to further ensure proper polarization filtering. An Erbium Doped Fiber Amplifier (EDFA) is used to amplify the optical signal inside the main loop cavity in order to compensate for the losses caused by the insertion losses of the different components inside the loop and ensure a high quality factor ($Q \sim 10^9$). A 100 GHz bandwidth filter is used to suppress the amplification of undesired modes. This EDFA is further used as a source of noise (see below).

The internal Mach-Zehnder interferometer of the intensity modulator is prone to thermal fluctuations, leading to slow drifts (on the order of several minutes) of the operation point. To compensate these drifts, the state of the intensity modulator is monitored by injecting optical power in the opposite direction of the main propagation direction using two circulators around the modulator. A low bandwidth (1 MHz) amplified photodiode signal monitors the transmitted optical power along this counter-propagating direction. This allows ensuring that intensity modulation is performed around mid-point, in a linear regime.

The heterodyne section consists of a 200 MHz upward frequency shifter to provide a Local Oscillator (LO). This LO is then amplified with a Semiconductor Optical Amplifier (SOA) before being mixed with the probe signal via a coupler. The heterodyne signal is then attenuated before detection with a 600 MHz bandwidth amplified photodiode. The photodiode signal is sampled by a 8 GHz bandwidth digitizer.

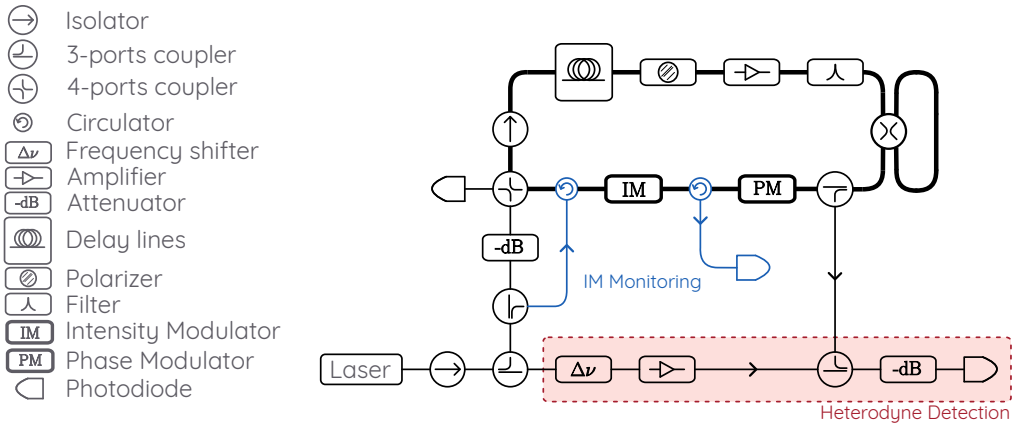

FIG. S1. Schematic representation of the experimental setup.

B. Calibration protocol

In order to compare different systems size with identical hopping strengths (and thus be able to obtain a relevant scaling), the hopping amplitudes α (phase modulation), β (intensity modulation) and ϵ (perturbation, phase modulation) must be calibrated for each value of the main loop's FSR. Indeed, when changing the main loop's length, and thus its FSR, we change the frequency of the voltage signal sent to the EOMs to produce the 1^{st} and 3^{rd} nearest-neighbor couplings. Since the electro-optics coefficient linking the voltage to the index of refraction changes as a function of the driving frequency, the amplitude of each Fourier component must be adjusted in order to generate identical hopping strengths. To do this, we perform the following calibration procedure.

First, we open the auxiliary (small) loop such that no mode of the main loop hybridizes with it. Therefore we obtain an infinite lattice of modes separated by the main loop's FSR. We then apply only the nearest-neighbor phase modulation (α), i.e. a Fourier component at exactly the FSR. This leads to a temporal band structure (as realized in previous implementations, including in Ref. 1) in the form of a perfect cosine function. A small deviation of the driving frequency from the FSR results in an effective electric field and distorted bands (associated to Bloch oscillations). This allows perfectly calibrating the FSR and, by inspection of the resulting bands' amplitude, to estimate the strength of the reciprocal nearest-neighbor couplings. We then drive the phase modulator only with a Fourier component at 3 times the FSR (3Ω). We still have a temporal band structure that is a perfect cosine function, but now with a period 3 times shorter (due to the increase of the lattice periodicity). The amplitude of this bands gives us a quantitative value of the perturbation ϵ.

Turning to the intensity modulation, we first calibrate its phase. This is important in order to account for any delay in the coaxial cables. Upon the presence of both the phase and intensity modulation, the band structure becomes asymmetric (see Fig. 2 (d) of the main text). We adjust the phase of the intensity modulation until the maximal intensity of the band structure occurs at the center of the rising edge to optimize the non-reciprocity. Importantly, we want the NHSE to accumulate toward lower frequencies. This allows accumulating the field, in frequency space, away from the LO frequency, and thus not having problems with negative frequencies in the heterodyne spectrum (see Fig. S2 (c)). Finally, we close the auxiliary loop and now drive the cavity with the nearest-neighbor phase (α) and amplitude (β) modulations to generate a NHSE in each N-site lattice. The amplitude of the intensity modulation is tuned until we obtain a specific slope of the field amplitude as a function of the lattice site (on a semilog vertical scale, see value chosen in the main text). This tuning of the NHSE, which is identical for all main loop's sizes, is chosen such that the total field amplitude circulating in the loop remains below a certain limit for the largest N, in order to prevent nonlinear dynamics. For the larger system sizes, this further requires lowering the input power in the loop. The responses reported in the main text are thus the output field normalized by the measured input field amplitude $|a_{in}|$.

C. Heterodyne detection

The main data of this work, reported in Figs. 3 and 4 of the main text, are taken from heterodyne spectra. This allows extracting the amplitude of the field in each frequency mode, notably at the edge of chains. As described above, heterodyne spectra are obtained by beating the signal radiating from the loop with a frequency shifted (200 MHz) copy of the laser. We accumulate the beating signal measured on a fast photodiode as the laser frequency is swept. Figure S2 (a) shows such spectrum. We clearly see the profile of the band's density of states. From this spectrum, we can select a thin slice of 2^{18}pts (b) around the center of the band to select data acquired with a minimal laser detuning. We finally perform a Fourier transform on this temporal region (c) with a resolution of $\sim$ 100 kHz over 600 MHz. A zoom on a region of interest (ROI), for positive frequencies, shows a clear HNSE on a single chain (d). In this case, $\epsilon = 0$ and the occupation of the neighboring chain is negligible.

In order to make sure that the sampled region in the heterodyne signal indeed corresponds to a region of minimal detuning, we can perform the same procedure for different slices of the full heterodyne signal. Figure S3 shows a heat map describing how the Fourier transform evolves as a function of the laser detuning, i.e. for different slices. We clearly see a maximal NHSE for $\Delta \to 0$, which allows identifying the ideal region for operating our system. This procedure is reiterated for each data presented in Figs. 3 and 4 of the main text to find the optimal operation point.

In the Supplementary Video appended, we show a summary of this procedure for every time window of the heterodyne spectrum measured for the case $N = 34$. We clearly see that for cuts outside of the band structure, the Fourier transform only consists of noise contributions that populate every chain identically, because the driving laser is out of resonance and does not couple to the loop. Then, when the laser becomes resonant, we see a clear NHSE in both chains, the driven one and its neighbor, which become maximal when the laser detuning is minimal.

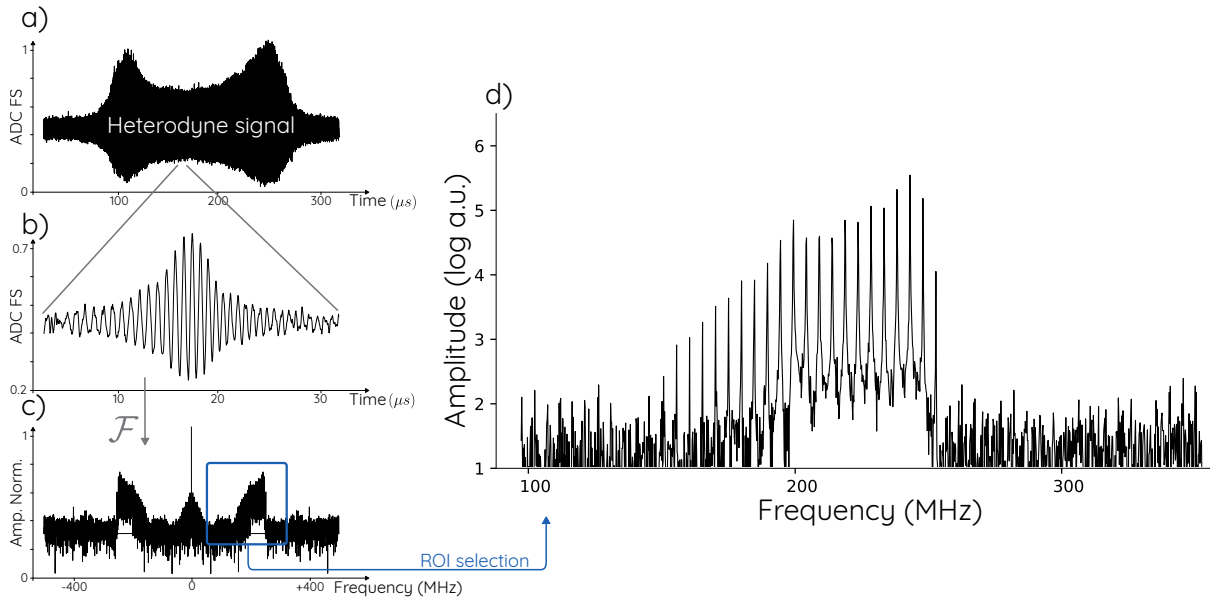

FIG. S2. (a) Time-resolved heterodyne signal as the laser detuning is scanned over a single band. (b) Sampling of the heterodyne signal around the region $\Delta = 0$. (c) Fourier transfom of the sampled signal with a zoom-in (d) on a single chain exhibiting a clear NHSE in frequency space.

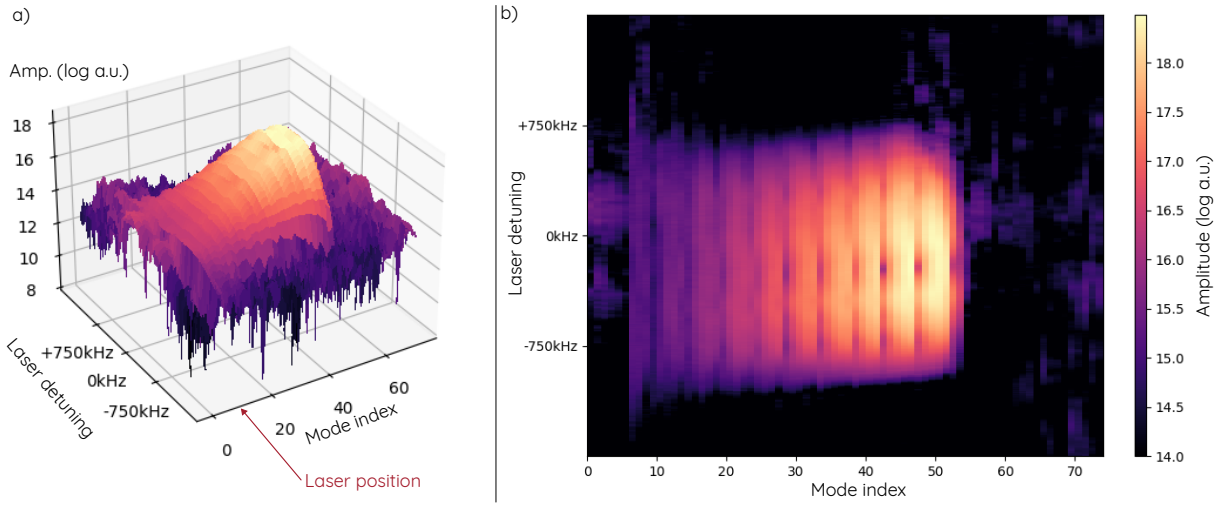

FIG. S3. Fourier transform of the heterodyne signal for slices of the temporal signal associated to distinct laser detunings over a single band. Panel (a) depicts a 3D mesh of this evolution, and panel (b) shows a top view. In both cases we see a clear NHSE in the pumped chain that evolves as a function of the laser detuning.

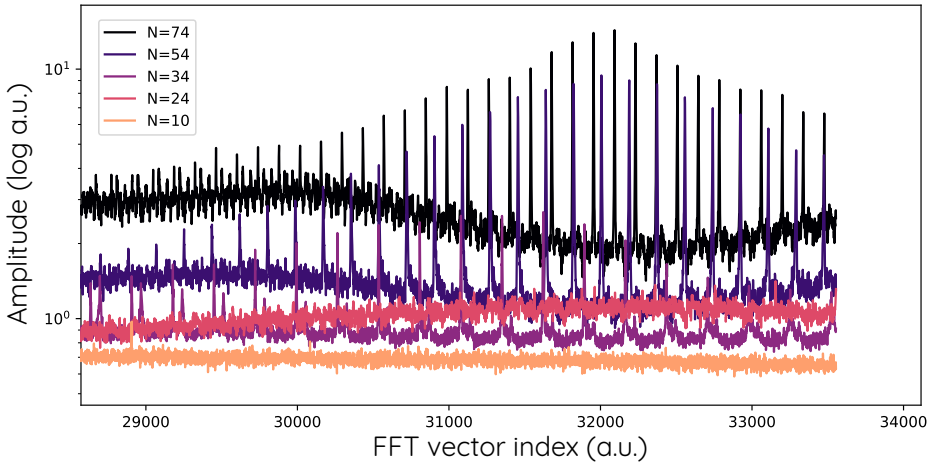

FIG. S4. Heterodyne spectra for different chain lengths where the input field is only incoherent noise. The occupation of the photonic modes is very clear, even though the laser is turned off, indicating that we indeed measure the photonic noise emitted by the EDFA.

D. Noise spectroscopy

One key aspect of our work is the ability to probe the system's response to environmental noise. This is obviously critical for assessing the SNR. In order to extract this response, we remove the coherent drive. Hence, the only source of electromagnetic field entering the loop (beside the vacuum shot noise that is too faint to overcome our photodiode's electrical noise) comes from the spontaneous emission of the EDFA embedded in the cavity which operates below the lasing threshold (as described above). This emission fulfills the condition of a white, uncorrelated noise. We then measure the response of this input noise in the heterodyne signal (similarly as described above). This is how the noise data presented in Fig. 3 (b) and 4 of the main text was acquired.

In order to distinguish this photonic noise from the electric noise of the detection system (photodiode + digitizer), we make sure that we see an occupation of the cavity modes of the loop. This indicates that the incoherent input field has indeed populated the modes of the cavity allowing to extract a scaling of this photonic noise specifically. Figure S4 shows a zoom-in of such heterodyne spectra where we clearly see the occupation of the cavity modes, except for the case $N = 10$ that is dominated by the electrical noise (see Fig. 3 (c) of the main text).

II. NUMERICAL SOLUTIONS OF THE LANGEVIN EQUATION

In order to confirm the signal and noise scalings observed experimentally (e.g. in Figs. 3 and 4 of the main text), we have modeled our system using the following set of coupled Langevin equations :

$$\dot{a}_i = i\,[H, a_i] - \frac{\gamma}{2} a_i - i\sqrt{\kappa} a_{in}^{(i)} \tag{S.1}$$

where a_i corresponds to the field amplitude in the i^{th} frequency mode of the cavity, γ is the optical lifetime, κ is the input-output coupling strength and $a_{in}^{(i)}$ is the driving field amplitude localized on the i^{th} site. The Hamiltonian H for a system consisting a succession of m N-site HN lattices is given by the following $mN \times mN$ matrix:

$$H = \begin{bmatrix} \ddots & & & & \\ & D & c & & \\ & c & D & c & \\ & & c & D & c \\ & & & c & \ddots \end{bmatrix}$$

where the m $N \times N$ diagonal blocks

$$D = \begin{bmatrix} 0 & J_+ & 0 & \epsilon & 0 & \dots & 0 & 0 & 0 & 0 & 0 \\ J_- & 0 & J_+ & 0 & \epsilon & \dots & 0 & 0 & 0 & 0 & 0 \\ 0 & J_- & 0 & J_+ & 0 & \dots & 0 & 0 & 0 & 0 & 0 \\ \epsilon & 0 & J_- & 0 & J_+ & \dots & 0 & 0 & 0 & 0 & 0 \\ 0 & \epsilon & 0 & J_- & 0 & \dots & 0 & 0 & 0 & 0 & 0 \\ \vdots & \vdots & \vdots & \vdots & \vdots & \ddots & \vdots & \vdots & \vdots & \vdots & \\ 0 & 0 & 0 & 0 & 0 & \dots & 0 & J_+ & 0 & \epsilon & 0 \\ 0 & 0 & 0 & 0 & 0 & \dots & J_- & 0 & J_+ & 0 & \epsilon \\ 0 & 0 & 0 & 0 & 0 & \dots & 0 & J_- & 0 & J_+ & 0 \\ 0 & 0 & 0 & 0 & 0 & \dots & \epsilon & 0 & J_- & 0 & J_+ \\ 0 & 0 & 0 & 0 & 0 & \dots & 0 & \epsilon & 0 & J_- & 0 \end{bmatrix} \tag{S.2}$$

describe the dynamics of the particle inside a single HN chain and the 2×2 off-diagonal blocks

$$C = \begin{bmatrix} \epsilon & 0 \\ 0 & \epsilon \end{bmatrix} \tag{S.3}$$

describe the coupling between neighboring chains. Here, the J_+ and J_- respectively describe the hopping amplitudes in the backward and forward directions, and ϵ the reciprocal 3^{rd} nearest-neighbor hopping amplitude inducing the perturbation coupling lattices.

The use of a $mN \times mN$ Hamiltonian captures the fact that our system is invariant under translation in frequency space. The eigenspectra, as depicted in Fig. 2 (b) of the main text, consists of a concatenation of an infinite number of N-site lattices (in the approximation of negligible dispersion). In order to compare the simulations with our experimental data, we extract the amplitude of the field (the a_i) in two chains located in the middle of our simulated frequency space. This captures the essence of the experiment, where we only select a subset of two connected chains and ignore the ones at higher and lower frequencies.

To describe the dynamics of the system upon injection of white noise and of a coherent state (to model the noise and signal respectively), we propagate Eq. S.1 in time with the drive terms consisting either of a random, spatially uniform field (for noise) or a well-defined, localized coherent amplitude.

In the first case, the random field is realized by generating a random array of driving fields $a_{in}^{(i)}$ (with i ranging from 1 to mN) by drawing, at each time step of the time evolution, random amplitudes and phases from a normal distribution such that, as explained in the main text,

$$\langle a_{in}^{(i)}(t) a_{in}^{(j)}(t') \rangle = n_{th} \delta_{ij} \delta(t - t'). \tag{S.4}$$

In the second case, the coherent field is generated by using a driving field localized on the first lattice site of the first chain of the subset considered, defined in the rotating frame as:

$$a_{in}^{(i)} = \delta_{i0} F_i e^{i\Delta_i t}. \tag{S.5}$$

with F_i the drive amplitude on the i^{th} mode and Δ_i its detuning with respect to the i^{th} mode. The factor δ_{i0} ensures that all the other lattice sites are undriven.

To confirm that the simulations are fully converged, we made sure that the results from the time evolution of Eq. S.1 with a coherent field matches its steady-state solution, i.e. solving the equations for $\dot{a}_i = 0$. These converged simulations are those that were used for all theoretical calculations presented in the main text, including the SNR

evolution as a function of N (Fig. 3 (c)) and of ϵ (Fig. 4) where the calculated signal is presented in shaded blue and the calculated noise in shaded orange.

The results of such simulations is presented in Fig. S5 for $m = 8$, $N = 34$ and $\epsilon = 0.1\frac{J_+ + J_-}{2}$. All simulations have reached the steady-state. Panel (a) shows the instantaneous solution, i.e. for a given time increment, when the system is driven with white noise. Panel (b) shows the same conditions, but a result that is time averaged over many increments to compare with the result in the experiment. In this latter case, one clearly sees the NHSE of noise which, on average, accumulates in every chain. This is compatible with the results presented in Fig. 3 (b) of the main text and Fig. S4. Panel (c) shows the solution when the system is driven with a coherent drive localized on the first lattice site of the 5^{th} chain. We clearly see the accumulation in the pumped chain, as well as in its right-side neighbors; we further see the accumulation in a third chain that is reduced by a factor ϵ^2.

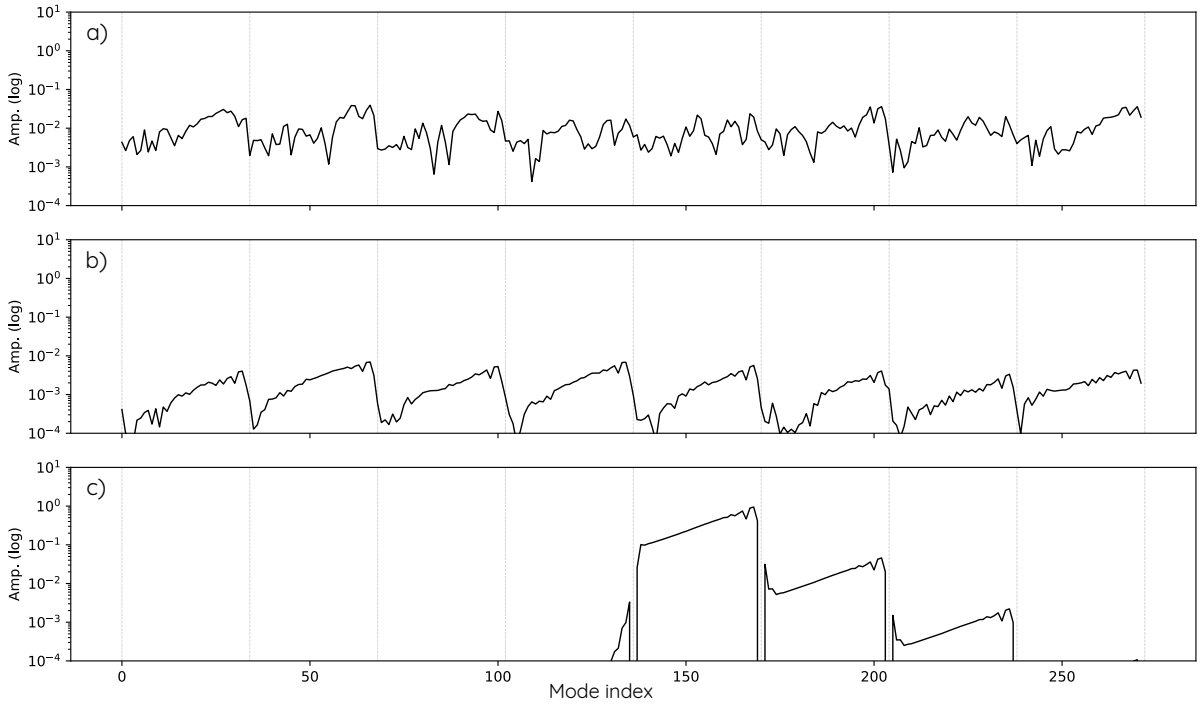

FIG. S5. **Simulated steady state.** Each simulation was performed with the exact same conditions: $m = 8$ chains of $N = 34$ sites and $\epsilon = 0.1\frac{J_+ + J_-}{2}$. a) Instantaneous state with only noise injected. b) Averaged steady state with noise. c) Coherent drive only, localized on the first site of the fifth chain. In each panel, the vertical dotted lines indicate the position of each chain.

III. e^{AN} SCALING OF THE NOISE

One of the main results of this work is the extraction of a scaling law for the noise in our system. This led to an exponential scaling of e^{AN} where N is the length of an individual HN lattice. As mentioned in the main text, this is distinct from the theoretical result proposed in Ref. [2]. In that previous work, noise could only enter in the system through the first lattice site of a BKC (see Fig. 1 (b) of the main text). As a result, in the limit $\epsilon \to 0$, the only contribution to noise in the output field consists of thermal noise occupying the input-output waveguide because, in that limit of a vanishing perturbation, all noise entering the BKC can't change quadrature and can't thus be amplified through a round-trip along the chain. As a result, in that limit and under these conditions, noise does not scale with the system size; in a regime where ϵ is not vanishingly small, this result does not hold and the noise does depend on the lattice size N.

In our frequency-encoding scheme, as in Ref. [3], noise can enter identically through all lattice sites. The above argument thus does not hold and we see a qualitatively different behavior. On key aspect that we observe is that noise follows exactly the same scaling as the amplitude profile of the NHSE in a single, isolated HN chain (e^{AN}). We can understand this scaling using the following argument.

Our system has translational invariance in frequency space, because we have an infinite succession (in the approximation of a non-dispersive medium) of HN lattices. This approximation is certainly valid over the relative low bandwidth considered in this work (typically $< 1\,\mathrm{GHz}$). Over this bandwidth, we can well approximate the noise (spontaneous emission from the EDFA) as uniform, i.e. white noise. Hence, since we have an eigenspectrum and a noise source that are translationally invariant in frequency space, the noise profile in each chain must me identical by symmetry. This is confirmed in the experiment and in simulations (see Fig. S5 (b)). Then, if we consider the processes by which noise can enter or exit a given chain that we label i, we have four contributions: A) noise entering/exiting from/toward the chain on the left, B) noise entering/exiting from/toward the chain on the right, C) noise emitted from the EDFA in each lattice site, and D) noise exiting the lattice through losses (γ) and the input-output coupler.

The rate at which noise enters or exits the i^{th} chain through the first two proecesses is given by:

$$\Gamma_A = \epsilon a_N^{(i-1)} - \epsilon a_1^{(i)} \tag{S.6}$$

$$\Gamma_B = \epsilon a_1^{(i+1)} - \epsilon a_N^{(i)}. \tag{S.7}$$

However, since $a_N^{(i-1)} = a_N^{(i)}$ and $a_1^{(i+1)} = a_1^{(i)}$ by translational invariance, those two contributions exactly cancel out. Therefore, the only net contributions come from processes C) and D) which are uniform in frequency and do not involve any neighboring chains. As a result the noise profile in each chain does not depend on the contributions from neighboring chains and scales identically as it would in a single, isolated chain, i.e. it follows the typical NHSE profile e^{AN}. This argument does not depend on the amplitude of ϵ and, as seen in Fig. 4 of the main text, the scaling of noise does not depend on that variable.

Finally, it is worth pointing out that if we had only one pair of HN chains, with noise uniformly entering each lattice site, as in the canonical model depicted in Fig. 1 (d) of the main text or in Ref. [3], this argument would fail as we would not have a translationally invariant spectrum: noise entering a given chain from the left would not necessarily cancel out with noise exiting to the right. In the BKC picture, that would mean that noise entering in the P quadrature from the X quadrature is not canceled out by noise exiting the P quadrature to another degree of freedom. However, in the limit $\epsilon \to 0$, the contributions $\Gamma_{A,B}$ vanishes and, even in this configuration, we should retrieve a e^{AN} noise scaling similar to the one we report in this work.

IV. EFFECT OF 3^{rd} NEAREST-NEIGHBOR COUPLINGS IN THE BULK OF THE CHAINS

One key distinction between our implementation of the coupled HN chains and the canonical one presented in Fig. 1 (d) of the main text (and equivalent to the BKC proposed in Ref. 2) is linked to the implementation of the perturbation linking the two chains. In the canonical model, only the last site of the first chain is linked to the first site of the second one. Here, as we explained in the main text, we added 3^{rd} nearest-neighbor couplings to couple the two chains, because the first and last lattice sites of each chain have low lifetimes. However, the perturbation we create does not only couple the last sites of the first chains to the first ones of the second chain. It couples, reciprocally, every mode of the chain to its 3^{rd} nearest-neighbor. It is important to mention that this modification does not qualitatively modify the behavior of the system.

In Fig. S6, we show the steady-state solutions of Eq. S.1, for a single chain, with and without ϵ (for $\epsilon = 0.1\alpha$, the largest value used in this work). In the bulk of each chain, we observe a similar exponential localization, indicating that the NHSE is not significantly affected by the presence of this reciprocal perturbation ϵ coupling every 3^{rd} nearest-neighbors. We considered in these calculations a drive detuning $\Delta_0 = 0.5\alpha$, similar to the one used for realizing Fig. 4 of the main text. Calculations showed that working in a perfectly resonant regime ($\Delta_0 = 0$, as was done for Fig. 3 of the main text) leads to a slight increase of the amplification factor A. The origin of this increased localization, for resonant excitations, is attributed to a modification of the trajectory $E(k)$ in the complex plane which slightly moves away from the origin and, in turn, decreases the skin depth. The impact of this perturbation on the bulk is an interesting point to explore in future works, as it could potentially lead to an enhanced SNR.

[1] A. Dutt, M. Minkov, Q. Lin, L. Yuan, D. A. B. Miller, and S. Fan, Nature Communications **10**, 3122 (2019), publisher: Nature Publishing Group.

[2] A. McDonald and A. A. Clerk, Nature Communications **11**, 5382 (2020), publisher: Nature Publishing Group.

[3] J. J. Slim, C. C. Wanjura, M. Brunelli, J. del Pino, A. Nunnenkamp, and E. Verhagen, Nature **627**, 767 (2024), publisher: Nature Publishing Group.

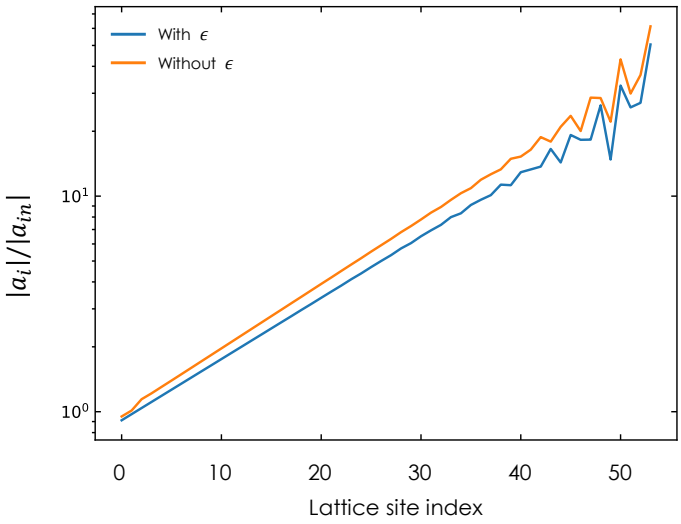

FIG. S6. Steady-state solutions of the Langevin equation for chains without (blue) and with (orange) 3^{rd} nearest-neighbor couplings.